PAPER

Check for updates

Synthesis of highly dispersed magnesium hydroxide and its application in flame-retardant EVA composites

Qinghua Chen,[a] Shiai Xu, (ID) *[ab] Rujie Li,[a] Beibei Sun,[a] Huidong Fang[b] and Qianqian Zhang[a]

Magnesium hydroxide (MH) is widely recognized as an environmentally friendly, halogen-free flame retardant and has been extensively applied in ethylene-vinyl acetate (EVA) copolymers. However, its poor dispersion in the polymer matrix and low flame retardant efficiency remain significant challenges. In this study, hexagonal magnesium hydroxide (MHz) with well-defined morphology, high specific surface area, and excellent dispersion was inventively synthesized *via* hydrothermal synthesis using sodium hydroxide (NaOH) and sodium carbonate (Na_2CO_3) as the hydrothermal medium. Three EVA composites filled with MHz and two different commercial magnesium hydroxides (MHx and MHy) were prepared *via* melt-blending, and their flame retardant and mechanical properties were systematically compared. The results indicate that the EVA composite containing 60 wt% MHz (EVA/MHz60) exhibits superior flame retardant performance, achieving a limiting oxygen index (LOI) of 49.2%, which is 53.8% and 9.1% higher than that of MHx and MHy, respectively. The UL-94 rating reached V-0. Furthermore, the peak heat release rate (PHRR) of EVA/MHz60 is significantly reduced to 150.6 kW m^{-2}, marking a 33.2% and 29.9% reduction compared to the EVA composite containing 60 wt% MHx (EVA/MHx60) and EVA composite containing 60 wt% MHy (EVA/MHy60), respectively. Additionally, the tensile strength of EVA/MHz60 is improved by 101.6% and 76.4% compared to that of EVA/MHx60 and EVA/MHy60, respectively. The improvement in tensile strength of the EVA/MHz60 composite can be attributed to the nanoscale and uniform dispersion of MHz with hexagonal morphology, which can enhance the interfacial adhesion with the EVA matrix, thus the flame retardant and mechanical properties of the composite can be improved simultaneously.

1 Introduction

Ethylene-vinyl acetate copolymer (EVA) is a widely used polymer material in everyday life, known for its excellent flexibility, good processability, and superior electrical insulating properties.[1,2] It is commonly applied in cable sheaths, construction, packaging, and transportation industries. However, due to its composition of carbon and hydrogen elements, EVA is highly flammable and releases harmful gases during combustion, significantly limiting its use in applications with stringent safety requirements.[3,4] To improve the flame retardancy of EVA, researchers have explored various flame retardants, such as aluminum hydroxide (ATH), expandable silicates, and organic phosphorous compounds. Among them, magnesium hydroxide (MH), an eco-friendly halogen-free flame retardant, is gaining attention for its high thermal decomposition temperature, low smoke emission, non-toxicity, and non-corrosiveness.[5–7] The incorporation of MH into the EVA matrix effectively integrates their

respective advantages, resulting in EVA composites with improved flame retardant properties and enhanced overall performance.

The particle size, morphology, and specific surface area of MH play a key role in determining its dispersion, interfacial compatibility, and flame retardant efficiency within polymer matrices.[8] The uniform dispersion of MH leads to a reduction in defects associated with particle agglomeration, thereby resulting in enhanced structural integrity and overall performance of the composite. Hornsby *et al.*[9] investigated the dynamic viscoelastic and shear flow properties of MH at 60% mass fraction in polypropylene. The results indicate that variations in both particle size and morphology not only influence the distribution of the filler within the matrix but also have a significant impact on the viscoelastic behavior and flame retardant properties of the material. Suihkonen *et al.*[10] investigated the effect of MH particle size on the flame retardancy, thermal, and mechanical properties of epoxy resin. They observed that, in comparison to micron-sized MH, nanoscale MH more effectively promotes char layer formation, thus enhancing the flame retardant properties of the composites.[11–13] High-performance MH flame retardants generally have particle sizes between 0.5 and 1.5 μm

[a]School of Materials Science and Engineering, East China University of Science and Technology, Shanghai 200237, China. E-mail: saxu@ecust.edu.cn

[b]School of Chemical Engineering, Qinghai University, Xining 810016, China

and a specific surface area less than 10 m^2 g^{-1}.[14] Due to these characteristics, optimizing their morphology continues to be a major challenge in improving flame retardant performance.

Currently, the synthesis methods for MH include direct precipitation,[15] solvothermal method,[16,17] mechanical grinding,[18] vapor deposition,[19] and electrochemical methods.[20] The direct precipitation method, while simple to operate, leads to MH with a morphology that is difficult to control and is prone to agglomeration. Although methods such as mechanical grinding, vapor deposition and electrochemical techniques can improve certain properties of MH, they are typically limited by high energy consumption, complex processes and high costs.[21,22] In contrast, the hydrothermal method, due to its high controllability, high crystallinity, and uniform particle size, has become a widely used synthesis approach.[23–25] During hydrothermal synthesis, the hydrothermal medium plays a key role in the crystallization growth kinetics and the control of morphology.[26,27] MH is classified within the hexagonal crystal system and is made up of Mg(OH)$_6^{4-}$ octahedra which are arranged in a closely packed hexagonal structure.[28] Under hydrothermal conditions, Mg(OH)$_6^{4-}$ growth units are formed with the participation of OH$^-$ ions, and their growth behavior is influenced by the pH, ion strength, and chemical environment of the hydrothermal medium.[28–31] For example, Xiang et al.[32] examined the effect of NaOH concentration in the hydrothermal system on MH growth and found that as the NaOH concentration increased, the average particle size of MH increased and its specific surface area decreased. Weng et al.[33] used NaCl and KCl as hydrothermal media and found that K$^+$ and Na$^+$ had a significant impact on the dissolution–recrystallization process of MH, resulting in changes to its surface polarity and morphology. Na$_2$CO$_3$ can effectively regulate crystal growth kinetics and morphology. Kuznetsov et al.[34] studied the spontaneous crystallization of rutile and found that the addition of Na$_2$CO$_3$ resulted in different growth rates of different crystal faces, which influenced the crystal size.[35] Based on the previous research of our group, we also found that the introduction of Na$_2$CO$_3$ not only provides Na$^+$ but also regulates the chemical environment of the hydrothermal system through CO$_3^{2-}$, optimizing the morphology and dispersion of MH.[36]

In this study, hexagonal plate-shaped magnesium hydroxide (MHz) flame retardant with uniform morphology was synthesized in a one-step hydrothermal process using NaOH as an alkaline mineralizer, MgCl$_2$ as the magnesium source, and Na$_2$CO$_3$ as the hydrothermal medium. Scanning electron microscopy (SEM) analysis confirms that MHz possesses a well-defined morphology, superior dispersibility, and improved interfacial compatibility. Compared to commercial MH fillers, MHz demonstrates a more uniform structure and enhanced compatibility with the matrix. Here, the flame retardant and mechanical properties of EVA/MH composites were analyzed systematically by some testing methods such as limiting oxygen index (LOI) test, vertical burning test (UL-94), Raman spectroscopy, etc. In addition, the flame retardant mechanism and smoke suppression of EVA/MH composites was further discussed. To evaluate the potential application of MHz in EVA composites.

2 Experiments

2.1 Materials

Magnesium chloride (MgCl$_2$), sodium carbonate (Na$_2$CO$_3$) and anhydrous ethanol were purchased from Titan Technology Co., Ltd (Shanghai, China). Ethylene-vinyl acetate copolymer (EVA 265, with a vinyl acetate content of 28 wt%) was obtained from Du Pont Co., Ltd (Shanghai, China). Sodium hydroxide (NaOH) was purchased from Aladdin Reagent Co., Ltd (Shanghai, China). Magnesium hydroxide-x (MHx) was purchased from Taixing Advanced Material Co., Ltd (Shandong, China). Magnesium hydroxide-y (MHy) was purchased from Albemarle Corporation (USA).

2.2 Preparation of samples

2.2.1 Hydrothermal synthesis of MHz. The 2 M NaOH, 1 M Na$_2$CO$_3$, and 1 M MgCl$_2$ were sequentially dissolved in deionized water in a beaker. The mixture was stirred for approximately 5 minutes before being poured into the polytetrafluoroethylene reactor. It was then placed into a blast drying oven and allowed to react at 180 °C for 3 h. Subsequently, it was removed from the blast drying oven, cooled to room temperature, and then subjected to vacuum filtration. Following this, the sample was dried at 80 °C in an oven to gain white powders.

2.2.2 Preparation of EVA/MH composites. Using melt blending method, MH fillers and EVA were blended using a torque rheometer (Rheocord 300P, Haake, Karlsruhe, Germany) operating at 60 rpm for 10 minutes and at 140 °C. The resulting mixtures were pressed to produce thin sheet samples, which were then further cut into LOI, UL-94, CCT and mechanical property specimens as required for testing. The synthesis route of MHz and EVA/MH composites is shown in Fig. 1. The sample information for this experiment is summarized in Table 1.

2.3 Characterization

2.3.1 X-ray diffraction (XRD). The crystal structure of MHz was analyzed using an Ultima IV X-ray diffractometer (Rigaku Corporation, Japan). The diffraction angle (2θ) ranged from 10 to 80°, with a scanning speed of 4 ° min^{-1}.

2.3.2 Surface morphology analysis (SEM). The morphologies of MH fillers and EVA/MH composites were examined using an S-4800 scanning electron microscope (Hitachi Ltd, Japan). Before testing, the powders were dispersed in anhydrous ethanol to prevent aggregation during drying. Before observing the fracture morphologies of EVA/MH composites, the materials were quenched in liquid nitrogen. The samples were subsequently coated with gold using a sputter coater. The acceleration voltage was set to 10 kV, and the acceleration current was 10 μA.

2.3.3 Specific surface area test. The specific surface area of MH fillers determined by N$_2$ adsorption in accordance with the BET method, using a TriStar II PLUS surface area and porosity analyzer (Micromeritics Instrument Corporation, Shanghai). Before to measurement, 12 h vacuum pre-treatment was conducted at 170 °C.
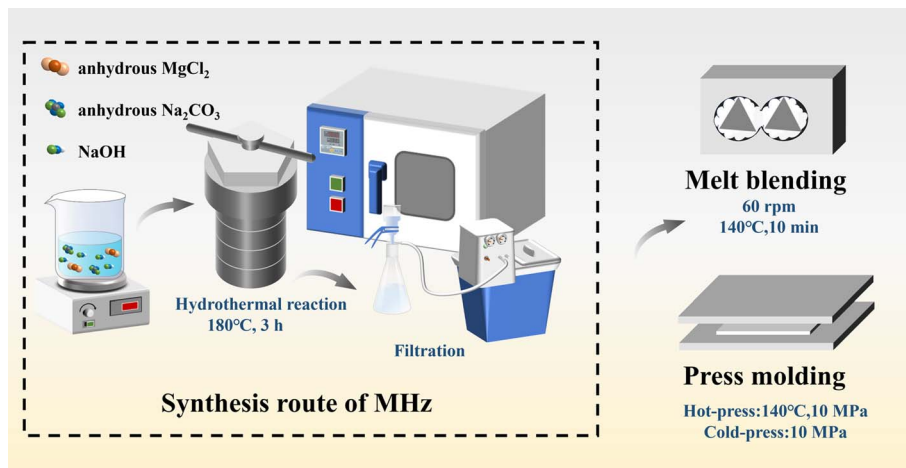
Fig. 1 Preparation routes of MHz and EVA/MH composites.

Table 1 Sample formulation and composition (wt%)

Samples		MH (wt%)	EVA (wt%)
Pure EVA		0	100
EVA/MHx[a]	EVA/MHx30	30	70
	EVA/MHx50	50	50
	EVA/MHx60	60	40
EVA/MHy[b]	EVA/MHy30	30	70
	EVA/MHy50	50	50
	EVA/MHy60	60	40
EVA/MHz	EVA/MHz30	30	70
	EVA/MHz50	50	50
	EVA/MHz60	60	40

[a] MHx: commonly used in industry, is widely applied in flame retardancy. [b] MHy: sourced from Albemarle Corporation (USA), known for its excellent flame retardant properties, representing high-performance flame retardants.

2.3.4 Thermogravimetric analysis (TGA). The thermal degradation behaviors of MH fillers and EVA/MH composites were analyzed using a TG209F1-GC thermal gravimetric analyzer (NETZSCH Instrument Manufacturing GmbH, Germany). The temperature ranged from 30 °C to 800 °C, with a heating rate of 10 °C min^{-1}, under a N_2 atmosphere.

2.3.5 Water contact angle (WCA) test. The surface contact angles of MH fillers were measured using a JC2000D1 contact angle tester (Zhongchen Digital Technology Equipment Co., Ltd, Shanghai). Prior to the test, the MH fillers were pressed into a disc with a diameter of 15 mm. A 3 μL droplet of deionized water was placed on the sample surface for contact angle measurement. Each sample was tested at least six different locations, and the average value was calculated.

2.3.6 Limiting oxygen index (LOI) test. The LOI values of EVA/MH composites were determined using an HG-JF-5 oxygen index tester (Nanjing Yixuan Instrument and Equipment Co., Ltd, China). Samples with dimensions of $100 \times 6.5 \times 3$ mm^3 were prepared following the standard ASTM D2863-77, and methane gas was used as the ignition source. Each sample was measured six times, and the average value was calculated.

2.3.7 Vertical burning test (UL-94). The UL-94 ratings of EVA/MH composites were determined using a HK-HVR horizontal-vertical burning tester (Zhuhai Huake Testing Equipments Co. Ltd, China) following the standard GB/T 2408-2021, utilizing specimens with dimensions of $125 \times 13 \times 3$ mm^3.

2.3.8 Cone calorimeter test (CCT). The CCTs of EVA/MH composites were performed using an EL3020 model (Kunshan Modisco Combustion Technology Co., Ltd, China) following ISO 5660. Specimens with dimensions of $100 \times 100 \times 3$ mm^3 were tested under radiation intensity of 35 kW m^{-2}.

2.3.9 Raman spectroscopy test. Raman spectroscopies of the residues from the combustions of EVA/MH composites were performed using an Invia Qontor micro-confocal Raman spectrometer (Renishaw, UK). A 532 nm helium-neon laser was employed for scanning in the range of 800–2000 cm^{-1}.

2.3.10 Mechanical property test. The mechanical properties of EVA/MH composites were evaluated using an E42.503 universal testing machine (MTS Industrial Systems Co., Ltd, Shenzhen). According to the standard GB/T 1040.2-2006, dumbbell-shaped standard specimens with a gauge length of 20 mm, a width at the narrow part of 4 mm, and a thickness of 2 mm were prepared. The tensile speed was set to 20 mm min^{-1}. Each sample was measured six times, and the average value was calculated.

3 Results and discussion

3.1 Characterization of the structure and morphology of MHz

XRD analysis was conducted on MH samples synthesized without and with Na_2CO_3 (Fig. 2a). The characteristic diffraction peaks at 2θ values of 18.5°, 38.1°, 50.8°, 58.6°, 62.3°, 68.2°, and 72.1° are assigned to the (001), (101), (102), (110), (111), (103), and (201) crystal planes of MH, respectively. A comparison with the standard diffraction pattern (PDF # 07-0239) confirms that the crystal structure matches the standard, verifying the successful synthesis of MH. The sharp peaks in the XRD pattern
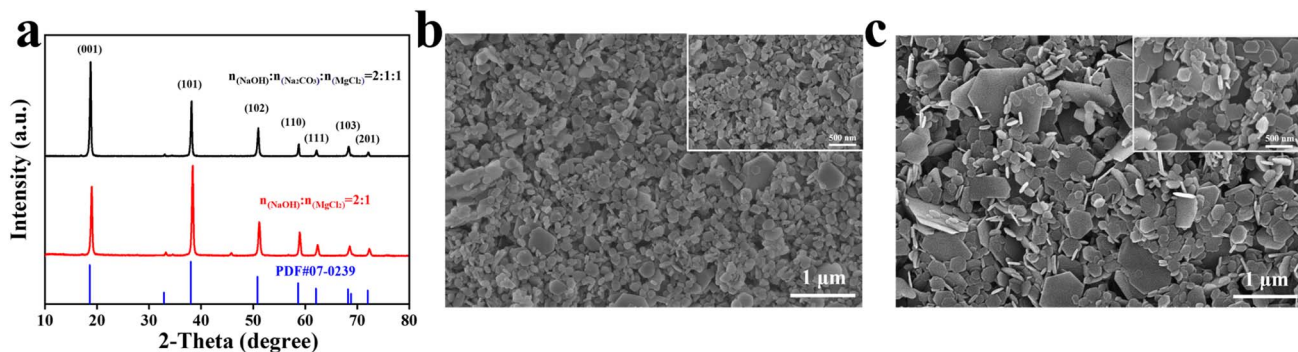
Fig. 2 XRD pattern (a) and SEM images of without Na$_2$CO$_3$ (b) and with Na$_2$CO$_3$ (c).

suggest that the synthesized MH exhibits high crystallinity. Following the addition of Na$_2$CO$_3$, the relative intensity ratio of the characteristic peaks ($I_{(001)}/I_{(101)}$) increased from 0.76 to 1.70, indicating that the crystal growth is more preferentially oriented along the (001) plane, which has weaker polarity, as opposed to the (101) plane, which has stronger polarity.[37] This change promotes the formation of a hexagonal plate morphology of MHz and significantly enhances the dispersion of the material (Fig. 2c). In contrast, Fig. 2b demonstrates that in the absence of Na$_2$CO$_3$, the synthesized MH displays poor dispersion, with most particles agglomerating, irregular in shape, and failing to form a well-defined hexagonal plate structure.

The fundamental growth units of MH, Mg(OH)$_6^{2-}$ octahedra, are primarily connected via face-to-face interactions along the (001) plane, making the structure more stable and easy to form a hexagonal lamellar structure. In contrast, growth along the (101) plane occurs through edge or vertex connections, leading to lower structural stability and a higher growth rate, which often resulted in irregular morphology.[28] The presence of CO$_3^{2-}$ ions further influences this process by selectively adsorbing onto the crystal surface, inhibiting the growth of the (101) plane while promoting the expansion of the (001) plane.[29–31]

3.2 Properties of MH fillers

To comprehensively evaluate the overall performance of MHz, two commercial MH types (MHx and MHy) were selected for comparison. Fig. 3 and Table 2 present the results. Fig. 3a–c show the morphologies of MHx, MHy, and MHz, respectively. MHx exhibits an irregular particulate morphology with significant
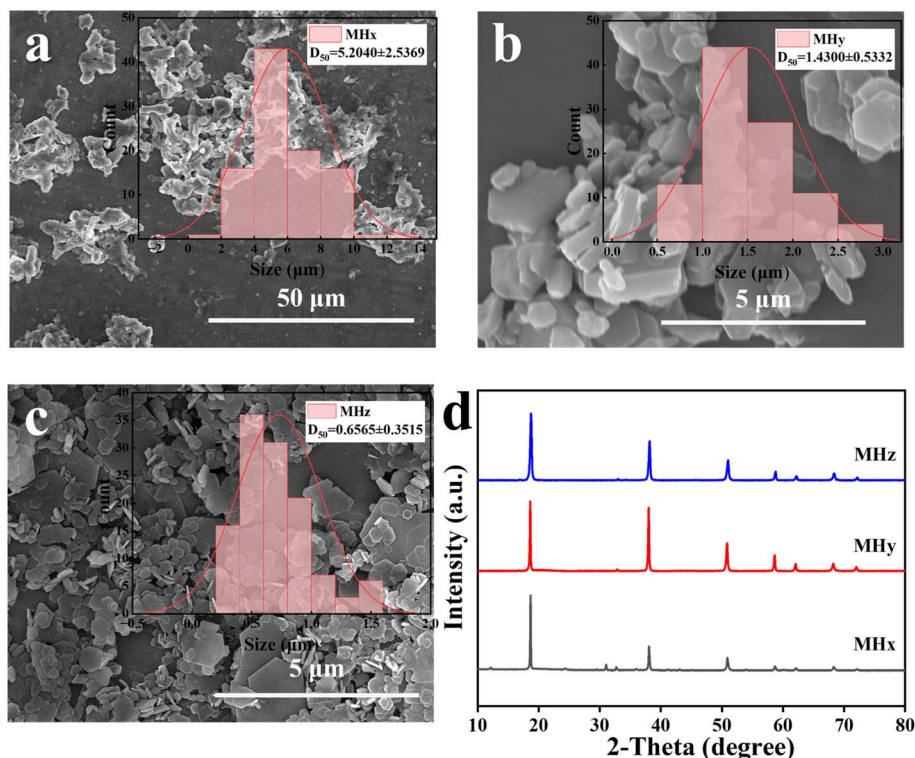

Fig. 3 Particle size distribution images from SEM of MHx (a), MHy (b), and MHz (c), and XRD patterns of MHx, MHy, and MHz (d).

Table 2 Particle size and specific surface area test results of MH fillers

Samples	Size (μm)	Specific surface area ($m^2 g^{-1}$)
MHx	5.204 ± 2.537	2.849 ± 0.009
MHy	1.430 ± 0.533	5.385 ± 0.180
MHz	0.657 ± 0.352	8.925 ± 0.654

aggregation, and its particle size is approximately 5.2 μm. MHy adopts a hexagonal plate-shaped structure, with thick plates predominantly stacked together, and a particle size of around 1.4 μm. Comparatively, MHz has the most regular morphology and good dispersion. The particle size of MHz is approximately 0.7 μm, and it possesses the highest specific surface area, reaching approximately 9.0 $m^2 g^{-1}$. Fig. 3d shows the XRD patterns of the three samples. MHx displays noticeable impurity peaks, indicating the presence of secondary phases or crystal defects. In contrast, no impurity peaks are observed in the patterns of MHy and MHz, suggesting higher purity. Further analysis shows that the $I_{(001)}/I_{(101)}$ ratio of MHy is 1.09, which is lower than that of MHz, indicating a stronger preferred orientation along the (001) plane in MHz and a more well-defined crystal morphology.

Fig. 4 shows the TG and TGA curves of MH (x, y, and z). As illustrated in Fig. 4, the residual content, falls within the error margin, aligns with the theoretical weight loss rate of 38.89% for the decomposition of MH to MgO. The initial decomposition temperature ($T_{5\%}$) of MHz is 344.50 °C, while the peak decomposition rate temperature (T_{max}) is 372.50 °C. In comparison, the $T_{5\%}$ values for MHx and MHy are 377.15 °C and 367.51 °C, respectively. The $T_{5\%}$ of MHz is reduced by 8.7% and 6.3% compared to those of commercial MH. This can be attributed to the effects of the morphology, particle size, and specific surface area of the filler on its $T_{5\%}$. Generally, smaller particle sizes and larger surface areas lead to decomposition at lower temperatures, as an increased surface area provides more active sites for thermal degradation.[38]

3.3 Compatibility

The interface compatibility of MH fillers within the EVA matrix was assessed by measuring WCAs to evaluate surface polarity

and hydrophilicity. Fig. 5 shows the WCA images of MH samples. It can be observed that the WCAs for MHx (Fig. 5a) and MHy (Fig. 5b) are 23.00° and 25.25°, respectively, indicating poor hydrophobicity and good wetting by water respectively. In contrast, MHz exhibits a WCA of 27.50° (Fig. 5c), suggesting reduced hydrophilicity and improved hydrophobicity compared to commercial MH fillers. The primary reason for this improvement is that the variability in surface roughness influences the contact angle. As a well-dispersed hexagonal plate-shaped sheet, MHz freely stacks in both horizontal and vertical directions. Such surface structures may trap air, creating additional air pockets between the water droplet and the surface, which causes the droplet to protrude, increases the contact angle, and ultimately enhances hydrophobicity.[39,40]

The SEM analysis results (Fig. 6) further confirmed the conclusions from the WCAs. The cross-section of pure EVA (Fig. 6a) appears smooth and homogeneous, suggesting an undisturbed internal structure devoid of fillers. However, the incorporation of MH with different morphologies into the EVA matrix resulted in a significant change in the cross-section structure of the material. In the EVA/MHx60 composite (Fig. 6b), a distinct interfacial gap exists between MHx and the EVA matrix. This gap implies that characterized by its higher hydrophilicity and irregular morphology, MHx fails to form a robust bond with the hydrophobic EVA matrix. Consequently, the material experiences weaker interfacial adhesion, leading to debonding. In contrast, the introduction of plate-shaped MH (MHy and MHz) results in a reduced interfacial gap, suggesting improved compatibility between the fillers and the matrix (Fig. 6c and d). However, in the EVA/MHy60 composite, pores and exposed plate-shaped MH caused by interfacial debonding are still observed. This could be attributed to the thicker plate-shaped morphology of MHy, which tends to aggregate and causes uneven dispersion in the matrix. In the EVA/MHz composite, the dispersion of MHz is uniform, with no noticeable interfacial gaps or debonding observed. The plate-shaped morphology of MHz appears to promote a near-seamless "encapsulation" with the EVA matrix, resulting in an almost indistinguishable interfacial boundary. The excellent interfacial adhesion performance is mainly attributed to the hexagonal
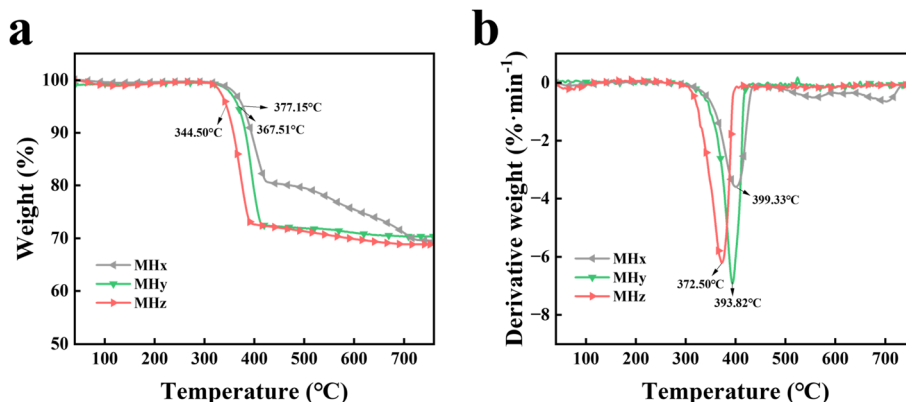

Fig. 4 TG (a) and DTG (b) curves of MH fillers.

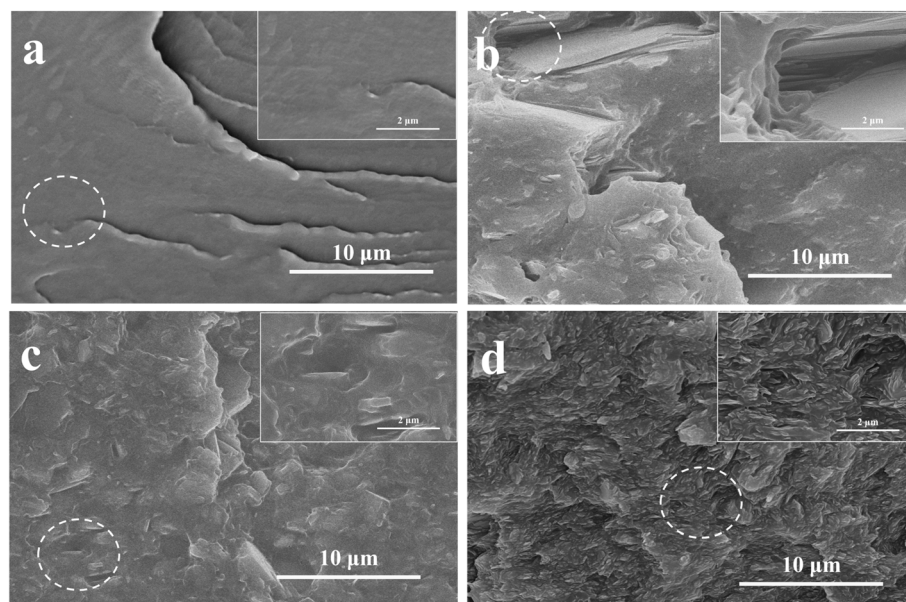Fig. 5 WCA images of MHx (a), MHy (b), and MHz (c).

Fig. 6 SEM images of pure EVA(a), EVA/MHx60 (b), EVA/MHy60 (c), and EVA/MHz60 (d) composites.

plate-shaped morphology of MHz and its nanoscale particle size. The large specific surface area of MHz facilitates strong interactions with the carbonyl groups (C=O) in the EVA matrix, resulting in enhanced interfacial compatibility. Moreover, the plate-shaped structure and excellent dispersion of MHz ensure its uniform distribution within the polymer matrix, thereby minimizing stress concentration and preventing agglomeration. This, in turn, enhances interfacial contact between the filler and the matrix, thus significantly improving the mechanical and flame-retardant properties of the composite.

3.4 Flame retardancy and smoke suppression

The LOI test results of the composites are shown in Fig. 7a. When the MH content was 30 wt%, the LOI of the EVA/MHz composite was 22.0%, which did not achieve the flame retardancy standard. When the MH content increased to 50 wt%, the LOI of EVA/MHz50 rose to 31.2%, showing improvements of 66.0%, 19.5%, and 4.7% compared to pure EVA, EVA/MHx50, and EVA/MHy50, respectively. Further increasing the MH content to 60 wt% resulted in an LOI of 49.2% for the EVA/
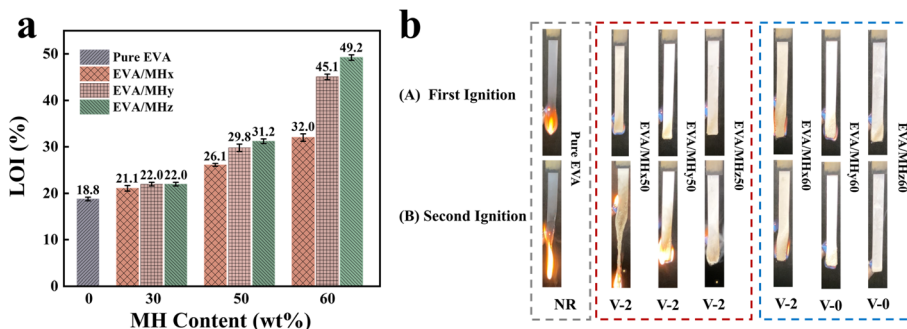

Fig. 7 LOI values (a) and UL-94 tests digital images (b) of pure EVA and EVA/MH composites.

Table 3 UL-94 results of pure EVA and EVA/MH60 composites

Samples	t_1 (s)	t_2 (s)	Spread	Cotton ignition	UL-94 rating
Pure EVA	11.58	>30	Yes	Yes	No rating
EVA/MHx50	22.66	4.14	No	Yes	V-2
EVA/MHy50	26.22	2.26	No	Yes	V-2
EVA/MHz50	28.01	1.98	No	Yes	V-2
EVA/MHx60	9.19	25.92	No	Yes	V-2
EVA/MHy60	2.33	5.26	No	No	V-0
EVA/MHz60	1.69	1.53	No	No	V-0

MHz60 composite, significantly surpassing the commercial counterparts, with improvements of 161.7%, 53.8%, and 9.1% compared to pure EVA, EVA/MHx60, and EVA/MHy60, respectively. LOI test shows that hexagonal sheet MH filler exhibits excellent flame retardancy compared to irregular MH fillers, where MHz has the best flame retardant properties. This is because the flaky MH forms a more effective physical barrier in the matrix, impeding the diffusions of flame and oxygen. In contrast, MHx, with its irregular morphology, exhibit poor dispersion due to uneven particle size distribution or aggregation, thereby negatively affecting its performance within the matrix.

UL-94 ratings for composites are typically assessed by observing the burn time of the specimen (t_1 and t_2) after the first and second ignition, whether the flame propagates to the fixture, and whether the molten droplets ignite the cotton pad. Fig. 7b and Table 3 present images of the specimen 2 s after ignition and the detailed test results, respectively. The test results show that pure EVA rapidly ignites after the first ignition, producing a significant amount of molten droplets, which

ignite the cotton pad; after the second ignition, the flame quickly propagates to the fixture, with the total after-flame time exceeding 30 s, thus failing to achieve a UL-94 flame retardancy rating. When the MH content is 50 wt%, the EVA/MH50 composite exhibits noticeable softening after the first ignition and burns more intensely after the second ignition, with molten droplets still igniting the cotton pad, resulting in a UL-94 rating of V-2. As the MH content increased to 60 wt%, both EVA/MHy60 and EVA/MHz60 composites attained a V-0 rating, demonstrating significant flame retardant performance. Among them, EVA/MHz60 demonstrates particularly exceptional performance, rapidly extinguishing within 10 s of ignition, with t_1 and t_2 being 1.69 s and 1.53 s, respectively. This may be attributed to the uniform distribution and good interfacial compatibility of the hexagonal plate-shaped morphology of MHz within the EVA matrix, significantly enhancing thermal isolation and resistance to the ignition of molten droplets. These results clearly demonstrate that, compared to other commercial MH fillers, MHz exhibits superior flame retardant performance in EVA composites.

Based on the LOI and UL-94 test results, and in conjunction with previous research,[41–44] the EVA/MH composite remains combustible when the MH content is 30 wt%. At 50 wt% MH, the UL-94 rating is only V-2. However, when the MH content increases to 60 wt%, the composite achieves a V-0 rating. Therefore, subsequent studies will focus on the flame retardant performance of the EVA/MH composite with 60 wt% MH content.

CCT is used to simulate the combustion behavior of polymer materials under real fire conditions. CCT tests on EVA/MH composites are shown in Fig. 8 and Table 4. Pure EVA is
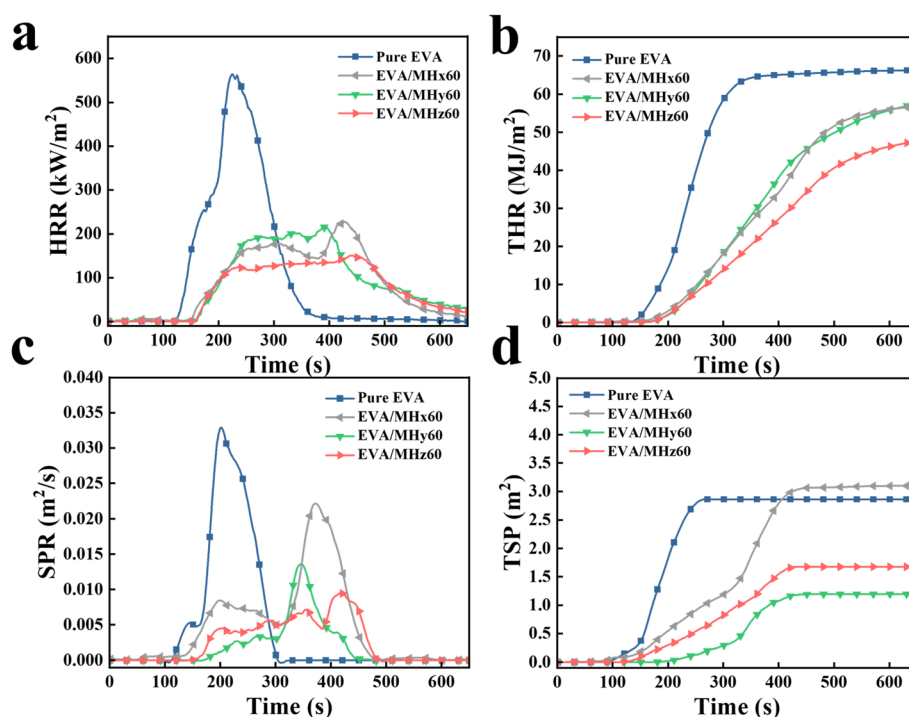

Fig. 8 HRR (a), THR (b), SPR (c), and TSP (d) curves of pure EVA and EVA/MH60 composites.

Table 4 CCT results of pure EVA and EVA/MH60 composites

Samples	TTI (s)	PHRR (kW m^{-2})	THR (MJ m^{-2})	PSPR (m^2 s^{-1})	TSP (m^2)	FPI (m^2 s kW^{-1})
Pure EVA	72	563.7	66.2	0.033	2.9	0.13
EVA/MHx60	91	225.6	56.7	0.022	3.1	0.40
EVA/MHy60	116	214.7	57.4	0.013	1.2	0.54
EVA/MHz60	134	150.6	47.5	0.009	1.7	0.89

flammable,[45,46] with a time to ignition (TTI) of 72 s and a peak heat release rate (PHRR) of 563.7 kW m^{-2}. For the EVA/MHz60 composite (Fig. 8a), the PHRR is much lower than that of the commercial EVA/MH60 composite. The TTI of EVA/MHz60 is 134 s, while its PHRR is 150.6 kW m^{-2}. Compared to EVA/MHx60 and EVA/MHy60, the PHRR of EVA/MHz60 is reduced by 33.2% and 29.9%, respectively. As seen in Fig. 8b, the total heat release (THR) of EVA/MHz60 is 47.5 MJ m^{-2}, 16.2% and 17.2% lower than that of EVA/MHx60 and EVA/MHy60. The peak smoke production rate (PSPR) of EVA/MHy60 is 0.013 m^2 s^{-1}, whereas EVA/MHz60 has 0.009 m^2 s^{-1}, a 30.8% reduction (Fig. 8c). Furthermore, Fig. 8d shows that the total smoke production (TSP) of EVA/MHz60 is 1.7 m^2, 45.2% lower than EVA/MHx60. The lower PSPR and TSP indicate enhanced smoke suppression by MHz. The fire performance index (FPI) for EVA/MHz60 is higher than that of the commercial EVA/MH60 composites, showing better fire safety (Table 4).

The excellent flame retardant performance is attributed to the nanoscale particle size of MHz, which leads to an increased specific surface area and enhanced compatibility with the EVA matrix, thereby facilitating more effective interfacial interaction. Also, MHz decomposes early in the thermal degradation process, creating a stable carbon layer on the surface. This carbon layer prevents oxygen and other flammable substances from reaching the matrix, which significantly hinders the spread of flames.[47]

3.5 Thermal stability

To study the thermal degradation behaviors of pure EVA and EVA/MH composites, TGA is performed under a N$_2$ atmosphere. The results are presented in Fig. 9. The TG curves reveal that the pure EVA undergoes a two-step decomposition process, beginning at 300 °C and concluding around 505 °C (Fig. 9a). The initial decomposition stage (300–395 °C) is mainly attributed to the decomposition of vinyl acetate, leading to the formation of the unsaturated polyene structure.[48] The second decomposition stage (395–505 °C) is primarily due to polyethylene chain scission.[49,50] During this process, the peak thermal degradation rate (R_{peak2}) of pure EVA is 20.84%/min, with the final char residue approaching 0, reflecting low thermal stability and flame retardancy.

The decomposition process of the EVA/MHz60 composite is quite similar to pure EVA, though noticeable differences appear in the thermal degradation behavior. A decrease of 4.24 °C in the initial decomposition temperature ($T_{5\%}$) is observed with the addition of MHz, suggesting an acceleration of early degradation. However, the peak decomposition temperatures (T_{peak1} and T_{peak2}) are increased to 352.02 °C and 472.13 °C, respectively. The char residue of EVA/MHz60 reaches 42.85%, as shown in Fig. 9a, which is higher than that of EVA/MHx60 and EVA/MHy60. This change is likely due to the peculiar decomposition mechanism of MHz. At around 330 °C, MHz decomposes quickly, producing MgO and H$_2$O. H$_2$O absorbs heat, lowering the temperature in the system, while MgO forms a dense layer on the polymer matrix surface.[51] Simultaneously, the generated MgO forms a dense protective layer on the polymer matrix surface, which, in conjunction with the char layer, effectively blocks the diffusion of oxygen and combustible gases, inhibiting further combustion.[52]

3.6 Char residue analysis

3.6.1 Char morphology analysis. The macro- and microstructures of the char residues after CCTs are analyzed using a digital camera and SEM. The digital images (Fig. 10) reveal
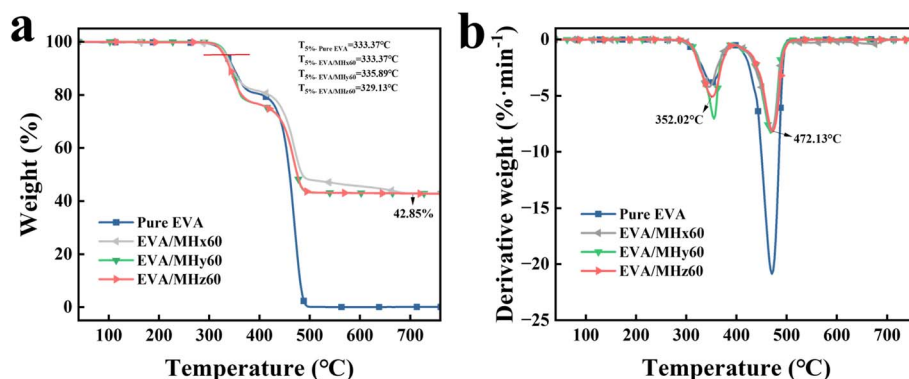

Fig. 9 TG (a) and DTG(b) curves of pure EVA and EVA/MH60 composites.

Fig. 10 Digital images of the char residues of EVA/MHx60 (a), EVA/MHy60 (b), EVA/MHz60 (c), and pure EVA (d).
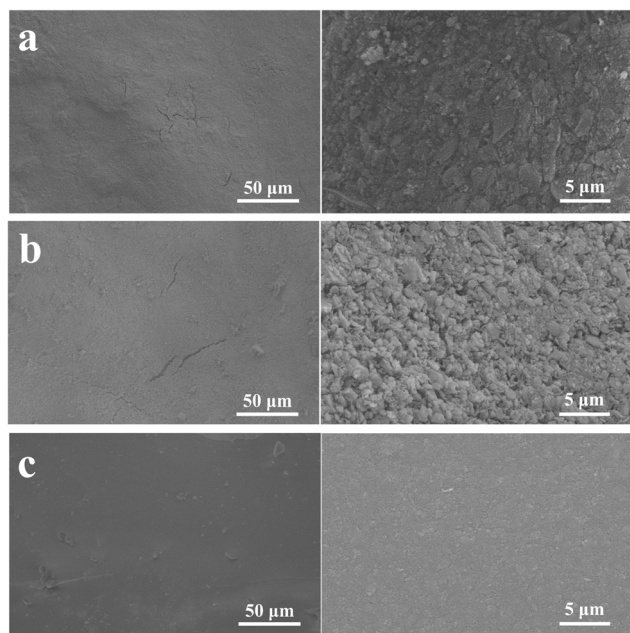

Fig. 11 SEM images of the char residues of EVA/MHx60 (a), EVA/MHy60 (b), and EVA/MHz60 (c) composites.

that the pure EVA has no residue after CCT test (Fig. 10d), and the surface of the residue after combustion in EVA/MHx60 (Fig. 10a) and EVA/MHy60 (Fig. 10b) exhibits significant fragmentation, with numerous irregular pores distributed across the macro surface. A large number of cracks are visible on the surface of the EVA/MHy60 composite, potentially due to its

lower filler dispersion and weaker interfacial bonding. In contrast, EVA/MHz60 also shows some fragmentation, but exhibits fewer surface pores, a darker overall appearance, and a more continuous char layer, suggesting the formation of a denser flame-retardant structure and improved post-combustion stability. SEM images support these findings, showing in Fig. 11. The surface structure of EVA/MHx60 (Fig. 11a) and EVA/MHy60 (Fig. 11b) is loose, with cracks and pores scattered throughout, creating clear pathways for heat transfer and combustible gas diffusion, which undermines the flame retardancy of the material. On the other hand, the microstructure of EVA/MHz60 is strikingly different, with a continuous, smooth surface and a tightly packed carbon layer (Fig. 11c). This dense carbon layer limits heat and gas exchange, considerably enhancing the thermal stability and flame retardancy of the material.

3.6.2 Raman spectroscopy. To investigate the graphitization degree of EVA/MH composites, Raman spectroscopy was used to analyze the residual char (Fig. 12). The D band reflects the presence of defects and disorder within the material, while the G band represents the degree of graphitization and the degree of order. The intensity ratio of these two bands (I_D/I_G) is commonly used to assess the graphitization degree; a lower I_D/I_G value indicates a higher degree of graphitization and better thermal stability of the carbon layer.[53] As shown in Fig. 12, the I_D/I_G values for EVA/MHx60 and EVA/MHy60 are 0.69 and 0.56, respectively (Fig. 12a and b), whereas the I_D/I_G value for EVA/MHz60 is 0.39 (Fig. 12c), indicating that EVA/MHz60 exhibits a higher graphitization degree. This finding is also consistent with the conclusion drawn from the digital images (Fig. 10).
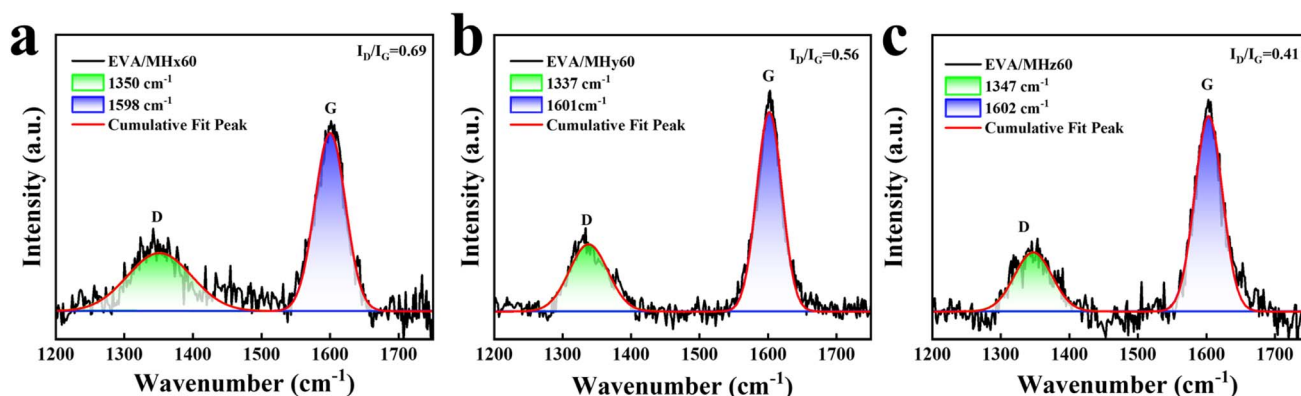

Fig. 12 Raman spectra of the char residues of EVA/MHx60 (a), EVA/MHy60 (b), and EVA/MHz60 (c) composites.

The analysis of the char residue indicates that the superior flame retardant performance of EVA/MHz60 is primarily due to the multifaceted properties of the MHz filler. On the one hand, the larger specific surface area of MHz and its good compatibility with the EVA matrix enhance the dispersion of the filler in the matrix, facilitating the more uniform formation of a dense carbon layer during decomposition. On the other hand, the MgO and H_2O produced during MHz decomposition act rapidly in high-temperature conditions. These compounds not only achieve a cooling effect through physical shielding and heat absorption but also strengthen and increase the density of the carbon layer through chemical reactions, effectively preventing heat transfer and the release of combustible gases. These combined factors contribute to the exceptional flame retardant performance of EVA/MHz60.

3.7 Flame and smoke suppression mechanism analysis

The flame retardant mechanism of EVA/MH composites can be inferred from the above analysis. When EVA/MH composites are exposed to high temperatures, their surfaces undergo significant and complex transformations.[32] Initially, EVA begins to melt and break down, eventually oxidizing into small molecules of volatile gases that can fuel the flame. At the same time, MH absorbs significant heat and releases substantial amounts of water vapor upon thermal decomposition, thereby reducing the surface temperature of the EVA composite. In addition, the water vapor released by MH can also cover the surface of material, decreasing the oxygen concentration in the combustion zone and suppressing combustion. The MgO generated by MH decomposition is covered on the surface of EVA, facilitating carbonization and forming the carbonaceous layer, which impedes the heat and oxygen infiltration, thereby further inhibiting combustion.[54]

Fig. 13 illustrates the specific processes involving MHz and commercial MH as flame retardants in EVA matrix. As seen in Fig. 13a, hexagonal flaky MHz with nanoscale particle size, high specific surface area and excellent dispersion exhibits layered distribution in the EVA matrix, causing the gas channels to become tortuous, thereby hindering the migration of combustible volatile gases produced by polymer decomposition, making it difficult for them to escape and provide fuel. As shown in Fig. 11a, b and 13b, commercial MH, with irregular morphology and a tendency to agglomerate, is unevenly distributed in the matrix, resulting in a porous, loose, and dispersed carbon layer on the EVA/MH composite surface. This allows flame heat and oxygen to penetrate the interior of the polymer, while combustible gases from polymer decomposition escape, fueling the flame. No dense protective layer forms on the composite surface. Therefore, once ignited, the flame retardant performances of commercial EVA/MH composites are inferior to that of EVA/MHz composites.

The disparity in flame retardant performance between MHz and commercial MH is primarily attributed to the significant differences in their filler characteristics. The hexagonal plate-shaped morphology of MHz, along with its excellent dispersibility, optimizes the distribution of the filler in the matrix. This also enhances the synergistic effects during the flame retardant process. Through its small particle size and high specific surface area, the interaction between MHz and the EVA matrix is improved, significantly contributing to the thermal stability and flame retardant efficiency of the composite material, thereby improving its overall performance.

3.8 Mechanical properties

As shown in Fig. 14, the tensile strength of EVA/MHz60 reaches 12.7 MPa, representing increases of 101.6% and 76.4% compared to EVA/MHx60 and EVA/MHy60, respectively. This significant improvement is primarily attributed to the hexagonal plate-shaped structure of MHz. Furthermore, the smaller particle size of MHz introduces the size effect, and the high specific surface area of the filler enhances the interfacial interaction with the matrix, thereby promoting better
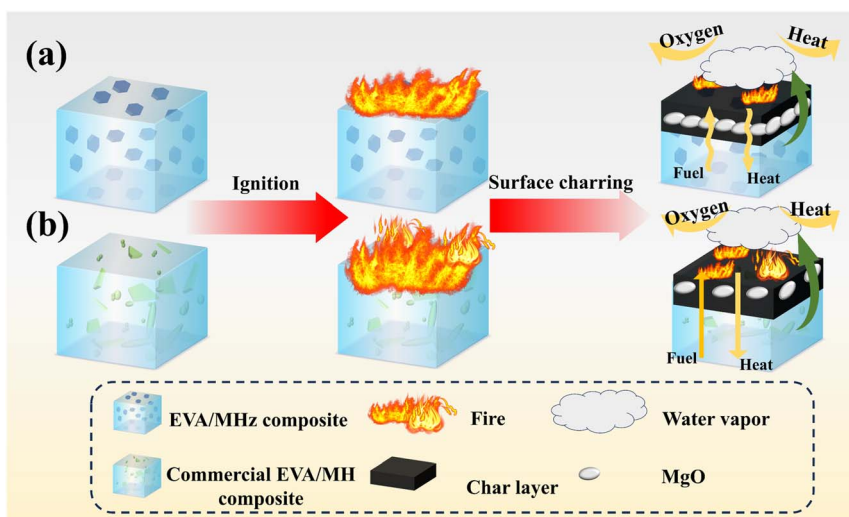

Fig. 13 Flame retardant mechanism of EVA/MHz (a) and commercial EVA/MH (b) composites.
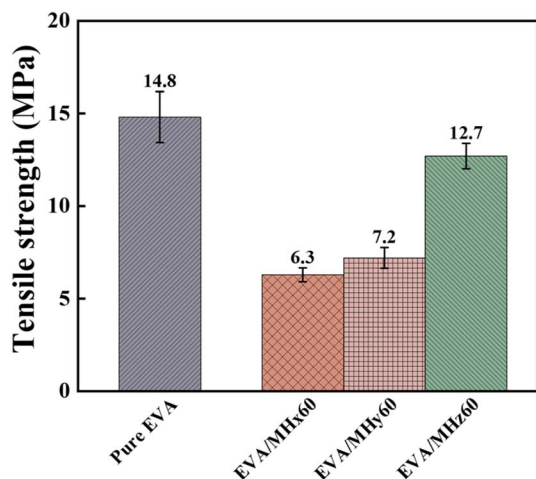
Fig. 14 Tensile strength of EVA and EVA/MH composites.

dispersion and interfacial compatibility in the EVA matrix, thus improving the tensile strength of the composite material. However, the tensile strengths of all EVA/MH composites decreased compared to that of pure EVA (14.8 MPa), indicating that the rigidity property of the inorganic filler weakened the mechanical properties of the matrix to some extent.

4 Conclusion

This study systematically compares MHz with commercial MH fillers MHx and MHy to verify the advantages of MHz in enhancing the flame retardant properties of EVA composites. The hexagonal plate-shaped MHz synthesized through the hydrothermal method exhibits a regular morphology, with a particle size of approximately 0.7 μm and a specific surface area of about 9.0 m^2 g^{-1}. It demonstrates excellent dispersion and compatibility in the EVA matrix, outperforming commercial MH fillers. At an identical filler loading (60 wt%), the LOI of EVA/MHz60 composites reaches 49.2%, representing increases of 53.8% and 9.1% compared to EVA/MHx60 and EVA/MHy60, respectively. Furthermore, it achieves a V-0 rating in the UL-94 flame retardancy test, showcasing exceptional flame retardancy. The CCT test further substantiates the flame retardancy advantages of MHz. Compared to EVA/MHx60 and EVA/MHy60, EVA/MHz60 reduces PHRR by 33.2% and 29.9%, respectively, and THR by 16.2% and 17.2%, signifying a substantial reduction in heat release and combustion intensity. Additionally, the PSPR of EVA/MHz60 decreases to 0.009 m^2 s^{-1}, 30.8% lower than that of EVA/MHy60, demonstrating superior smoke suppression. In conclusion, MHz, owing to its nanoscale particle size, high specific surface area, regular morphology, and excellent thermal decomposition characteristics, exhibits superior flame retardant and smoke suppression performance in EVA composites, surpassing commercial MH fillers. The systematic comparison conducted in this study affirms the high efficiency of MHz as a flame retardant and offers novel insights for the design and application of high-performance MH flame retardants, holding significant industrial application potential.

Data availability

All data used will be made available by the corresponding author on reasonable request.

Author contributions

Validation, formal analysis, investigation, resources, data curation, and writing-original draft were done by Qinghua Chen; conceptualization, writing-review & editing, and supervision were done by Shiai Xu; conceptualization was also done by Rujie Li; project administration was done by Beibei Sun, Huidong Fang and Qianqian Zhang.

Conflicts of interest

The authors declare that there is no conflict of interest.

Acknowledgements

References

1 Y. Yu, S. Tang, D. Feng, Y. Xie, F. Wu, D. Xie, Y. Mei and H. Huang, *Polym. Degrad. Stab.*, 2024, **225**, 110777.
2 Y. He, Z. Zhang, H. Ke and Y. Lu, *Chem. Eng. J.*, 2023, **470**, 143940.
3 J. Ji, D. Ni, Y. Shi, Z. Yang, M. Ma, S. Zhu and X. Wang, *J. Appl. Polym. Sci.*, 2024, **141**, e55505.
4 Z.-Y. Hu, S. Xu, H.-B. Zhao and Y.-Z. Wang, *J. Appl. Polym. Sci.*, 2019, **136**, 47243.
5 M. Yao, H. Wu, H. Liu, Z. Zhou, T. Wang, Y. Jiao and H. Qu, *Polym. Degrad. Stab.*, 2021, **183**, 109417.
6 L. Dun, Z. Ouyang, Q. Sun, X. Yue, G. Wu, B. Li, W. Kang and Y. Wang, *Polymers*, 2024, **16**, 1471.
7 X.-W. Cheng, K. Xuan, J.-P. Guan, W. Liu and G. Chen, *Colloids Surf., A*, 2023, **676**, 132287.
8 R. Li, B. Sun, L. Dang, T. Pan, J. Xu and S. Xu, *J. Appl. Polym. Sci.*, 2023, **140**, e54371.
9 P. R. Hornsby and A. Mthupha, *J. Mater. Sci.*, 1994, **29**, 5293–5301.
10 R. Suihkonen, K. Nevalainen, O. Orell, M. Honkanen, L. Tang, H. Zhang, Z. Zhang and J. Vuorinen, *J. Mater. Sci.*, 2012, **47**, 1480–1488.
11 H. Fang, T. Zhou, X. Chen, S. Li, G. Shen and X. Liao, *Particuology*, 2014, **14**, 51–56.
12 X. Shi, H. Chen, Y. Sun, X. Song and J. Yu, *Cryst. Res. Technol.*, 2022, **57**, 2200014.
13 J. Jakić, M. Jakić and M. Labor, *J. Therm. Anal. Calorim.*, 2020, **142**, 2099–2110.
14 M. Ren, M. Yang, S. Li, G. Chen and Q. Yuan, *RSC Adv.*, 2016, **6**, 92670–92681.
15 A. Samodi, A. Rashidi, K. Marjani and S. Ketabi, *Mater. Lett.*, 2013, **109**, 269–274.

16 H. Wu, B. Luo, C. Gao, L. Wang, Y. Wang and Q. Zhang, *J. Dispersion Sci. Technol.*, 2020, **41**, 585–591.

17 S. Jamil, S. R. Khan and M. R. S. A. Janjua, *J. Chin. Chem. Soc.*, 2018, **65**, 1495–1503.

18 Y. Liu, J. Li and Q. Wang, *J. Compos. Mater.*, 2007, **41**, 1995–2003.

19 P. S. Das, A. Dey, M. R. Chaudhuri, S. Roy, N. Dey, A. K. Mandal and A. K. Mukhopadhyay, *Surf. Eng.*, 2012, **28**, 731–736.

20 H. Amrulloh, W. Simanjuntak, R. T. M. Situmeang, S. L. Sagala, R. Bramawanto, A. Fatiqin, R. Nahrowi and M. Zuniati, *Inorg. Nano-Met. Chem.*, 2020, **50**, 693–698.

21 X. Liu, C. Liao, L. Lin, H. Gao, J. Zhou, Z. Feng and Z. Lin, *Surf. Interfaces*, 2020, **21**, 100701.

22 G. Balducci, L. Bravo Diaz and D. H. Gregory, *CrystEngComm*, 2017, **19**, 6067–6084.

23 Z. Rajabimashhadi, R. Naghizadeh, A. Zolriasatein and C. Esposito Corcione, *Nanomaterials*, 2023, **13**, 454.

24 A. Sierra-Fernandez, L. S. Gomez-Villalba, O. Milosevic, R. Fort and M. E. Rabanal, *Ceram. Int.*, 2014, **40**, 12285–12292.

25 X. Sun and L. Xiang, *Mater. Chem. Phys.*, 2008, **109**, 381–385.

26 J. C. Jumas, A. Goiffon, B. Capelle, A. Zarka, J. C. Doukhan, J. Schwartzel, J. Détaint and E. Philippot, *J. Cryst. Growth*, 1987, **80**, 133–148.

27 H. Poignant, L. Le Marechal and Y. Toudic, *Mater. Res. Bull.*, 1979, **14**, 603–612.

28 Q. Wang, L. Xiang, Y. C. Zhang and Y. Jin, *J. Mater. Sci.*, 2008, **43**, 2387–2392.

29 Q. Yuan, Z. Lu, P. Zhang, X. Luo, X. Ren and T. D. Golden, *Mater. Chem. Phys.*, 2015, **162**, 734–742.

30 H. Ma, Z. Chen and Z. Mao, *Vacuum*, 2013, **95**, 1–5.

31 L. Bai, M. Wang, X. Liang, W. Zhao and S. Dai, *J. Cryst. Growth*, 2024, **643**, 127810.

32 L. Xiang, Y. C. Jin and Y. Jin, *Guocheng Gongcheng Xuebao*, 2003, **3**, 116–120.

33 C. Weng, X. Song, H. Zhu and X. Luo, *RSC Adv.*, 2024, **14**, 14640–14647.

34 V. A. Kuznetzov, *J. Cryst. Growth*, 1968, **3–4**, 405–410.

35 B. Litvin and V. Popolitov, *Hydrothermal Synthesis of Inorganic Compounds*, Nauka, Moscow, 1984, pp. 52–59.

36 K. Chai and S. Xu, *Adv. Powder Technol.*, 2022, **33**, 103776.

37 Y. Lv, L. Bai, Y. Ma and L. Zhao, *Materials*, 2024, **17**, 1956.

38 J. Kalfus and J. Jancar, *Compos. Interfaces*, 2010, **17**, 689–703.

39 S. Lan, D. Zhu, L. Li, Z. Liu, Z. Zeng and F. Song, *Surf. Interface Anal.*, 2018, **50**, 277–283.

40 Z. Rajabimashhadi, R. Naghizadeh, A. Zolriasatein, S. Bagheri, C. Mele and C. E. Corcione, *J. Coat. Technol. Res.*, 2023, **20**, 1815–1834.

41 Y. Ma, M. Chen, N. Liu, P. Dang, Y. Xu, X. Chen, Z. Wang and J. He, *J. Thermoplast. Compos. Mater.*, 2016, **30**, 1393–1413.

42 R. Li, S. Xu, J. Xu, T. Pan, B. Sun and L. Dang, *Polymers*, 2023, **15**, 2575.

43 W. Zhao, C. K. Kundu, Z. Li, X. Li and Z. Zhang, *Composites, Part A*, 2021, **145**, 106382.

44 H. Gui, X. Zhang, Y. Liu, W. Dong, Q. Wang, J. Gao, Z. Song, J. Lai and J. Qiao, *Compos. Sci. Technol.*, 2007, **67**, 974–980.

45 Y. Liu, B. Li, M. Xu and L. Wang, *Materials*, 2020, **13**, 1251.

46 J. Liu, K. Zhou, G. Tang, B. Wang, Z. Gui, R. K. K. Yuen and Y. Hu, *Polym. Compos.*, 2018, **39**, 238–246.

47 J. Reuter, L. Greiner, F. Schönberger and M. Döring, *J. Appl. Polym. Sci.*, 2019, **136**, 47270.

48 M. C. Costache, D. D. Jiang and C. A. Wilkie, *Polymer*, 2005, **46**, 6947–6958.

49 D. p. Jena, B. Mohanty, R. K. Parida, B. N. Parida and N. C. Nayak, *Mater. Chem. Phys.*, 2020, **243**, 122527.

50 P. Gu and J. Zhang, *Iran. Polym. J.*, 2022, **31**, 905–917.

51 G. Camino, R. Sgobbi, A. Zaopo, S. Colombier and C. Scelza, *Fire Mater.*, 2000, **24**, 85–90.

52 A. Witkowski, A. A. Stec and T. R. Hull, *Polym. Degrad. Stab.*, 2012, **97**, 2231–2240.

53 B. Xu, W. Ma, X. Bi, L. Shao and L. Qian, *J. Polym. Environ.*, 2019, **27**, 1127–1140.

54 X. Li, J. Zhang, X. Yang, Y. Jin, Z. Lv, S. Lan, D. Zhu and L. Dang, *J. Appl. Polym. Sci.*, 2024, **141**, e55354.